Photodegradation of Rhodamine B by CeO$_2$-CuO Binary Composite Nanoparticles Synthesized by Self-Combustion Method

[1]W. Bouchal, [1]F. Djani*, [2]A. Martlnez-Arias, [1]Dj. E. Mazouzi, [3]S. Rezgui

[1]*Molecular Chemistry and Environment Laboratory, Mohammed KHIDER University Biskra, BP 145 RP, Biskra, 07000, Algeria.*
[2]*Instituto de Catálisis y Petroleoquímica, CSIC, C/Marie Curie 2, Campus de Cantoblanco, 28049 Madrid, Spain.*
[3]*Laboratory of Photonic Physics and Multifunctional Nanomaterials, Physics Department, Faculty of Exact Sciences, Mohamed Khider University, Biskra, Algeria.*
f.djani@univ-biskra.dz*

Summary: A novel binary composite CeO$_2$-CuO has been synthesized via self-combustion method employing cerium and copper nitrates, and glycine as fuel, and was investigated as photocatalyst to test the photodegradation of Rhodamine B (RhB) dye with visible light. The nanocomposite has been characterized by thermogravimetric analysis (TGA) to establish the temperature of calcination, X-ray diffraction (XRD) structural and morphologic analysis, scanning electronic microscopy (SEM) and energy-dispersive X-ray spectroscopy (EDS), which enables the chemical characterization/elemental analysis of materials, the photoluminescence (PL), UV-Vis Diffuse reflectance spectroscopy (UV-Vis DRS), measurement of specific surface (S_{BET}) by N$_2$ adsorption and temperature programmed reduction (TPR) analysis. The XRD diffractogram shows that the composite is majorly composed of 65.2% CeO$_2$ and 34.8 % CuO. The nanoscaled-tested samples have an average particle size of 40 to 65 nm. The energy gap of the material as synthesized was 2.05 eV. The TPR curves show 2 peaks of hydrogen consumption in the sample, corresponding to the decrease (reduction) of CuO particles caused by their interaction with CeO$_2$.The results of the photocatalytic tests show 28% conversion in the photodegradation of RhB organic pollutant during 180 min under visible light. The CeO$_2$- CuO material could be reused for treatment of wastewater during several cycles, which demonstrates its stability for the process.

Keywords: CeO$_2$/CuO, Photocatalytic activity, Recyclability, Rhodamine B, Self-combustion visible light.

Introduction

Water covers 71% of the planet's surface, yet only 0.002% of it is considered accessible to humans [1]. Because of the industrial development in almost every society. Water pollution has become one of the major problems threatening our planet. Pollution of water resources is most dangerous to the environment. This environmental pollution can be characterized by the presence of chemical products, microorganisms, industrial waste and organic dyes. Organic colourants are increasingly used in different industry sectors, including textiles, paper, chemical cosmetics, etc. [2, 3]. However, 30-40 % of these dyes remain in wastewater and thus causing serious health and environment issue. [4] One of such organic dyes which is very stable and very difficult to be degrade, is Rhodamine B. Rhodamine B (RhB) is a water-soluble cationic pigment [5].It is frequently employed as a tracer in pathological, histological, and microbiological sciences [6, 7]. RhB may cause cancer, respiratory infections, and dermatitis, among many other issues [8, 9]. Because of its difficulty to become degraded, its removal constitutes still a challenge and we need to find an effective,

economical and ecofriendly way for it [10, 11]. Various techniques have been used for the elimination of the organic dyes. Photocatalytic oxidation has recently received a great deal of attention owing to its ease of use, improved efficiency, high durability, and absence of secondary pollutants [12, 13].Photocatalytic materials operate by means of generating oxidant radicals via low-energy photon absorption and, compared to other procedures, could reduce material usage and treatment costs due to catalyst recycling [14]. For such purpose, researchers are currently concentrating their efforts on the development of novel semiconducting materials that work as photocatalysts [15].

Metal atoms make up oxide semiconductors, which have a broadband gap and allow visible light to be used for assisting a chemical reaction. Several studies on multi-metal oxide (MMO) nanoparticles have been conducted to determine their suitability as optical, catalytic, adsorbent, and wide-bandgap semiconductor materials oxide [16]. With a band gap

---

energy of 3.2 eV, pure CeO_2 has been identified as an essential nanomaterial to be used in catalysis [17], fuel cells [18], and hydrogen storage materials [19], photocatalysis [20], and other activities. Because of its propensity to flip between reduced and oxidized states when the gas phase oxygen content varies, ceria has had a lot of success in redox and combustion catalysts [21-23]. The introduction of a second metal into the ceria lattice may enhance structural stress and result in the formation of lattice defects, so changing the material into an excellent semiconductor [24]. CuO is a notable p-type semiconductor with only a small band gap (1.2 eV). CuO is one of the most important industrial materials with several applications, including gas sensors, electrochemical properties [25], photovoltaics, and photocatalytic degradation [26].In turn, the control of properties of the catalyst in the form of nanoparticles is currently an important scientific concern due to their unique properties and possible application. Various methods like self-combustion sol-gel [27], co-precipitation [28] are used to prepare nanoparticles. The self-propagating high temperature synthesis (SHS), which was discovered around 1967 by Mezhanov, Shkiro, and Borovinskay, is an exothermic chemical process that is generally very rapid and self-sustaining. [29]. The combustion-based synthesis of solid materials is classified as gas-phase combustion synthesis because of the physical aspects of metal precursors [30]. In this respect, the purpose of this search is to evaluate the photocatalytic ability of a binary composite CeO_2-CuO and examine its feasibility of recycling with the visible-light photodegradation of Rhodamine B. Using the self-combustion method, CeO_2-CuO nano powder will be synthesized. Next, thermogravimetric analysis (TGA), X-ray diffraction (XRD), scanning electronic microscopy (SEM), UV-Vis Diffuse reflectance spectroscopy (UV-Vis DRS), measurement of S_{BET}, and TPR analysis will characterize the produced binary oxide. Finally, the photocatalytic activity for the photodegradation of RhB under visible light for 180 minutes will be examined.

Experimental

Synthesis and characterization of CeO₂/CuO (CCU):

Synthesis

The sample was prepared by self-combustion method [31]; the reaction of the synthesis can be presented as follows:
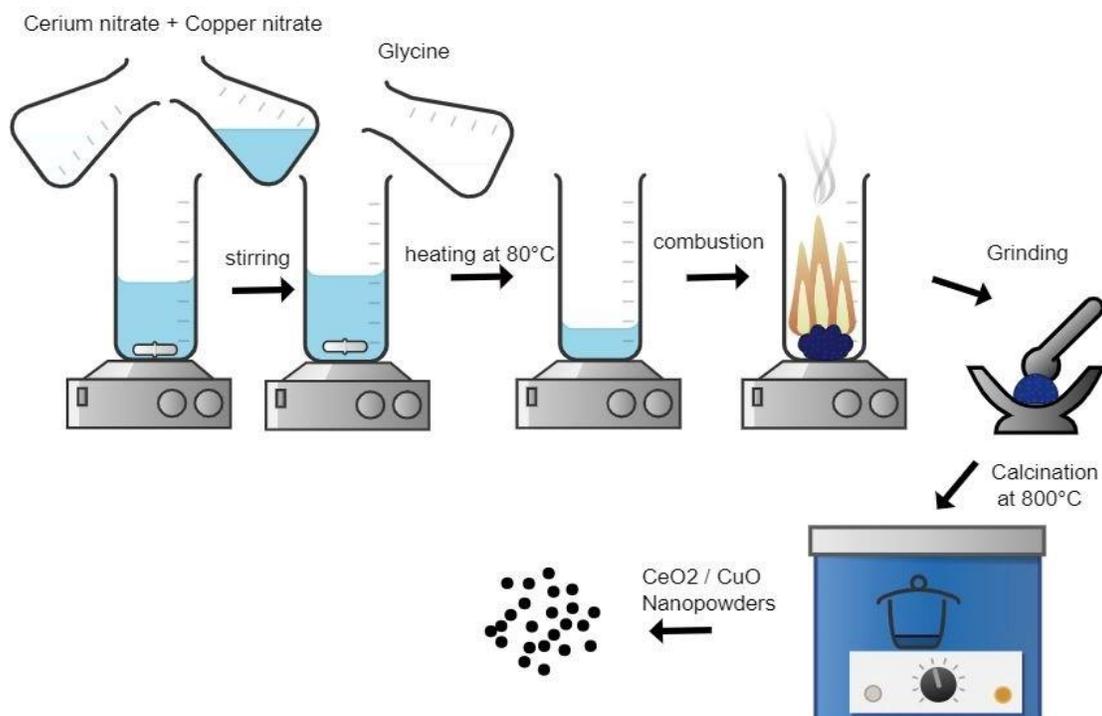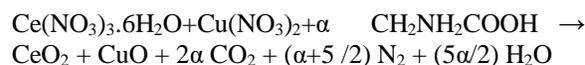
$Ce(NO_3)_3.6H_2O + Cu(NO_3)_2 + \alpha \quad CH_2NH_2COOH \rightarrow CeO_2 + CuO + 2\alpha\ CO_2 + (\alpha+5/2)\ N_2 + (5\alpha/2)\ H_2O$

Fig. 1: Diagram of different steps in the synthesis of CeO_2-CuO.

Fig. 1 shows the procedure used to synthesize CeO$_2$-CuO using self-combustion technique. Cerium and copper nitrates Ce (NO$_3$)$_3$.6H$_2$O, Cu (NO$_3$)$_2$, glycine CH$_2$NH$_2$COOH from sigma Aldrich, and distilled water were employed as reactants and solvents, respectively.

As fuel, 2.54 g of glycine was dissolved in minimum volume of distilled water. Then, 13.02 g of Cerium nitrates and 06.51 g of Copper nitrates were prepared separately in an aqueous solution and were added to the solution of glycine prepared. The obtained solution was stirred and heating at 80 °C during 50 - 60 min a brown gel was formed. After that, the temperature of the heating was increased to the maximal temperature until combustion occurred with the formation of cinder. After combustion in air and grinding, the combusted gel became a fine powder. Finally, the powders were thermally treated for 5 hours at 800 °C (5°C/min) in ambient atmosphere.

Characterization

The thermal degradation process of the sample precursor (before the calcination at 800 °C) was performed by thermogravimetric analysis (TGA) using a PerkinElmer TGA7 apparatus from 25 to 900 °C, with a heating rate of 10 °C/min in air. The crystallographic information of the sample powders was obtained with a powder X-ray diffractometer (Bruker AXS D8 advance) employing Cu-K_α radiation (λ =1.542 Å) in the 2θ range from 5° to 85°. The crystalline phases were identified in comparison to the JCDDS standard using the X pert highscore program.Infrared Transmission Spectrum (FTIR) was performed on a Fourier transform spectrophotometer PerkinElmer VATR 2, in the range 4000-400 cm-1.Surface morphology was explored on model VEG33TESCAN scanning electron microscope. Using an energy dispersive X-ray EDAX analyzer connected to SEM, the elemental composition was identified.A Carry 60 UV-VIS spectrophotometer was used for the optical band gap (Eg) measurement using the UV-VIS diffuse reflectance spectra of the synthesised sample. Horiba Fluoromax-4 spectrofluorometer was used to obtain the photoluminescence spectrum of the as prepared sample.
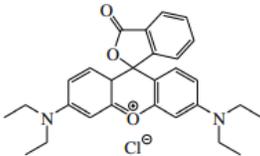
The N$_2$ adsorption/desorption isotherms were acquired using a Micrometrics apparatus model ASAP-2000. The sample was previously subjected to outgassing overnight at 140°C. Using the BET approach on the nitrogen adsorption/desorption isotherm, the specific surface area (S$_{BET}$) was determined. The Barrett-Joyner-Halenda (BJH) Method was used to measure the sample's pore size distribution (pore diameter and pore volume).The automated apparatus Micromeritics Autochem II 2920, which is equipped with a mass spectrometer and a TCD to examine the hydrogen concentration, is used to perform the TPR analysis.

Photocatalytic test

The photodegradation of Rhodamine B dye solution by visible light was invistigated using a self-combustion-prepared CCU nanoparticles catalyst. Table 1 lists the structure and properties of RhB. In this study, a homemade photoreactor equipped with 4*3W visible lamps was used. The concentration of the Rhodamine B was 2.087*10^{-8} mol/l.

Table-1: Rhodamine B Characteristic's [32].

Hill Formula	C$_{28}$H$_{32}$ClN$_2$O$_3$
Molar mass	480.018 g/mol
Mp/°C	165
Solubility	15 g/l
Soluble in	s H2O, EtOH, eth, bz, xyl
Structure formula	

Before performing the different analyses, the degradation of RhB was tested without photocatalyst with and without light, for 24 h. No change in the absorbance of RhB was found in these blank tests.
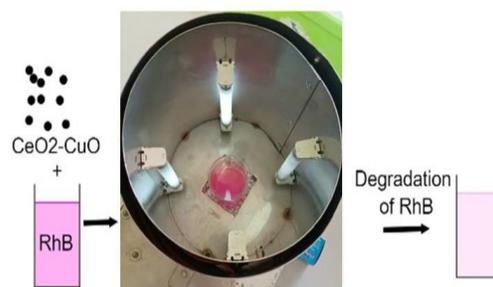

Fig. 2: Photocatalytic degradation of RhB by CeO$_2$/CuO prepared.

20 mg of photocatalyst was introduced to 40 m of RhB solution (0.5 mg/ml) in each test. The solution was magnetically stirred in the dark for 30 minutes to guarantee dispersion of the catalyst and achieve adsorption/desorption equilibrium, and was then exposed to visible light Fig. 2. The mixture was continuously stirred to maintain homogeneity, and the evolution of the degradation during 3h was

measured every 30 min. Before performing the spectrophotometric analysis, centrifugation and filtration were done to remove the nanoparticles.

Using a Uviline 9400 spectrophotometer, the absorbance of the supernatant solution was measured.

The photodegradation percentage was calculated using the equation:

$$\% \ of \ degradation \ = \frac{C_0 - C_t}{C_0} \times 100$$

where C_0 and C_t are, respectively, the initial and the measured concentrations of RhB in the solution at $\lambda_{max} = 554 \ nm$.

Results and Discussion

TGA analysis

To establish the most adequate conditions of calcination, TGA analysis was carried out on the CCU precursor powder. Fig. 3 illustrate the results.

Basically, five decomposition processes were identified, and there was a total weight decrease of 12.5 % (0.36 mg). Throughout the process of heating from room temperature (RT) to 900 °C under atmospheric air. The first loss of weight occurs between 25 to 175 °C. Which corresponds to the desorption of adsorbed or hydration water. The

second one, between 175 and 275 °C, is related to the combustion reaction and combined decomposition products of the metal nitrates [33]. From 275 to 370 °C, we notice a mass gain that would be apparently caused by incorporation of oxygen from air to the material. From 370 to 600 °C the weight loss is probably related to the decomposition of carbonates or related complexes and final formation of the oxides [34]. Above this temperature, only weak loss is detected until 900°C, particularly above 800 °C, which could be related to small reduction of the material given the high oxygen mobility expected for this type of material. On the basic of these results.800 °C is considered an adequate calcination temperature to get the final oxide material.

XRD analysis

The X-ray diffractogram of the sample thermally treated at 800 °C shows that the studied composite is a compound of cerium and copper oxides. Fig. 4 shows the XRD pattern of the synthesized oxides (calcined at 800 °C). The diffraction peaks for the cubic phase of CeO_2 (space group Fm3m -225-) appear at 2θ diffraction angles of 28.55° 33.08°, 47.49°, and 56.35° (ICDD 98-062-1710) for most intense ones. In turn the diffraction peaks at angle 2θ of 35.57°, 38.73°, and 46,28° correspond to the monoclinic phase of CuO (space group C12/C1 -15-) (ICDD 98-001-6025).
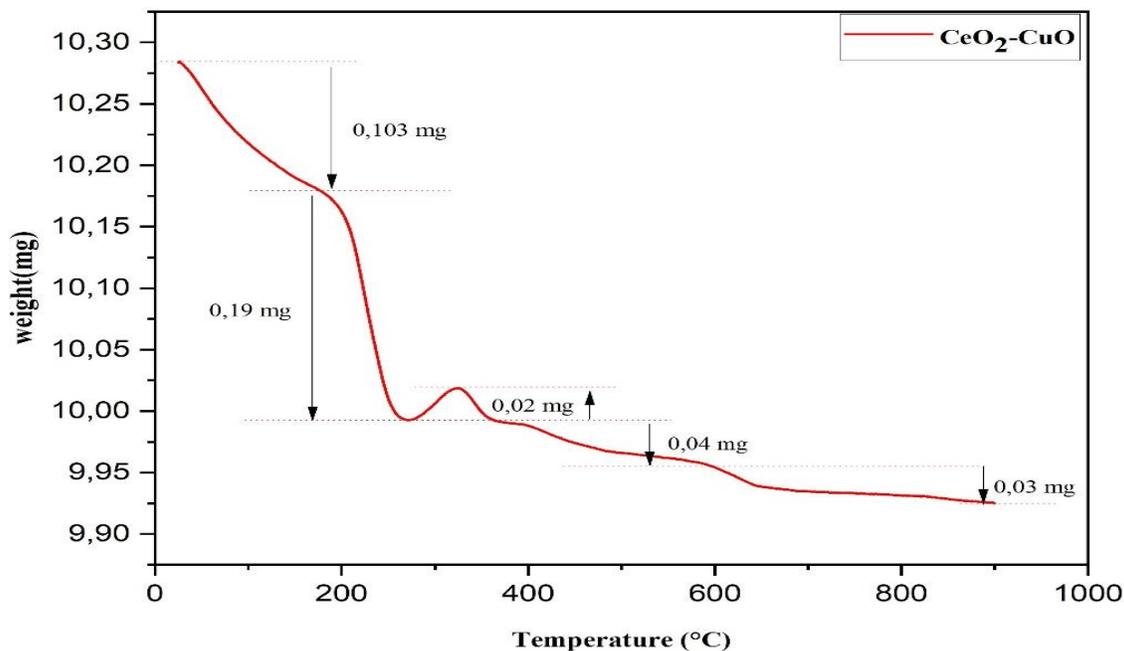

Fig. 3:   TGA curve of CeO_2-CuO powders as prepared.

Table-2: Refined lattice parameters of the as prepared CCU sample.

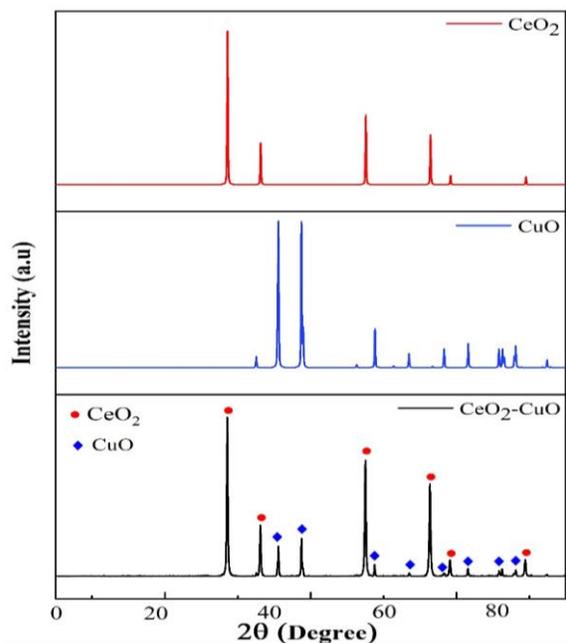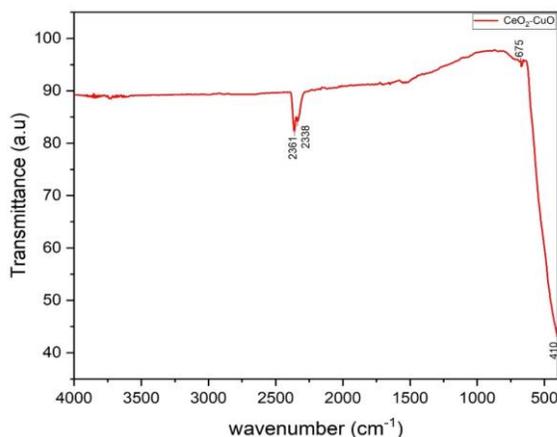| Oxide	Composition (%)	Crystal system	a/Å	b/Å	c/Å	α/°	β/°	γ/°	crystalline size (nm)
CeO₂	65.2	Cubic	5.41082	5.41082	5.41082	90	90	90	41.6
CuO	34.8	Mnoclinic	4.68676	3.42125	5.130925	90	99.44	90	65.1

Fig. 4:   XRD pattern of the as synthetized oxides.

Rietveld refinement shows that the composite is majorly composed of 65.2 % of cerium oxide while and 34.8% copper oxide. Refined lattice parameters are presented in Table-2.

Fig. 5:   CeO₂-CuO Infrared spectrum.

By using the Scherer formula, the crystallite size of the as-prepared sample was calculated [35]:

$$D = \frac{0.89\lambda}{\beta \, cos \, cos \, \theta}$$

The calculated average crystalline sizes of Cerium and Copper oxides were of 41.6 nm and 65.1 nm, respectively.

IR analysis

Fig. 5 represents the FTIR spectrum of the CCU sample as-prepared.

The binary composite includes two metal-oxygen (M-O) vibrations at wave number range of 4000-400 cm^{-1}. According to several reports of [36], and [37], The peaks around 410 and 675 cm^{-1} are attributed to Cu-O and Ce-O stretching vibrational mode of corresponding oxides: CuO and CeO₂ respectively. The peaks appeared at 2361, 2336 cm^{-1} due to the carbon dioxide molecule which is most likely adsorbed on the substrate [38].

SEM and EDS analysis:

In order to investigate the morphology of the binary oxide, SEM images are shown in Fig.6-a**.** In the micrograph, large agglomerates with non-uniform forms of particles, rough and heterogeneous surface structures [39], were observed.

In addition to SEM, energy-dispersive X-ray spectroscopy analysis was performed to validate the synthesis of CCU nanoparticles (NPs).

Both Ce and Cu can be seen in the synthesized composite nanostructure in the EDS spectrum with different percentages. The percentage of 83.1 % and 16.9 % are related to Ce and Cu respectively. Details of the EDS spectrum (percentage abundance of elements in composite) of the CeO₂/CuO NPs values measured in weight percentage are listed in the table included in Fig.6-b.

Photoluminescence analysis:

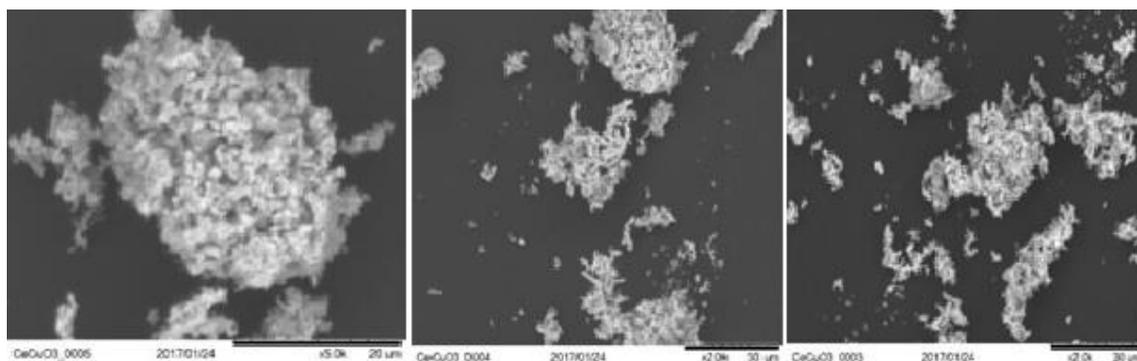At room temperature, with an excitation wavelength at λext =290 nm, the PL emission spectrum of CCU was determined.

As mentioned, CeO₂ and CuO are crystalized in cubic (fluorite) and monoclinic structures, respectively. Defects, especially oxygen vacancies, influence the electronic composite structure and the valance states of Ce and Cu ions. In this case, the cerium can exist in both states Ce^{4+}

(4f0) and Ce^{3+} (4f1); hence, emission processes in the case of cerium tetravalent state involve charge transfer from the ligands exited levels O2p to the 4f of Ce4+ ions ground states via the ligand to metal charge transfer (LMCT) mechanism [40]. In the case of CuO monoclinic structure, defects reduce some Cu^{2+} ions to the Cu^{1+} oxidation state and create localized states in the band gap, which can be involved in the relaxation process pathway [41]. The spectrum at Fig. 7 exhibits seven peaks and three shoulders due to a superimposing of different emission sources and mechanisms. At 396 nm and 476 nm, respectively, two major emission peaks were found for CeO_2 and CuO, respectively. Weak emission bands were also found at 421,450 and 482 nm. CeO_2 emission may be associated with the transition from Ce 4f band to O 2p band (valance 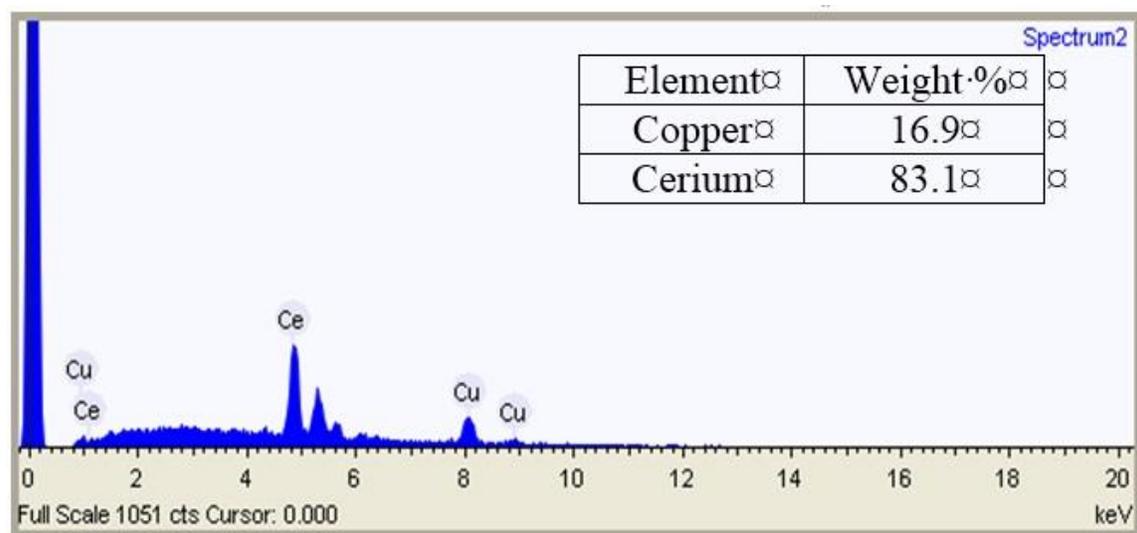band) [42]. The strong near-band edge (NBE) in the ultraviolet region due to the recombination of electron-hole pair of free excitation[43].peaks in the 400-500 nm (421,450 and 482 nm)range correspond to deep emission levels due to oxygen vacancies and Cu interstitials[44]. Both PL peaks at 350 nm and 550 nm might be attributed to defects, which include oxygen vacancies with levels of electronic energy underneath the 4f band. [45].

UV-Vis DRS analysis:

In the case of a semiconducting solid, UV-vis spectroscopy enables the calculation of the band gap (Eg); i.e., the minimal energy necessary to promote an electron from the valence band (VB) to the conduction band (CB), even during electronic process that occurs in the material following interaction with light [46].

(a)

(b)

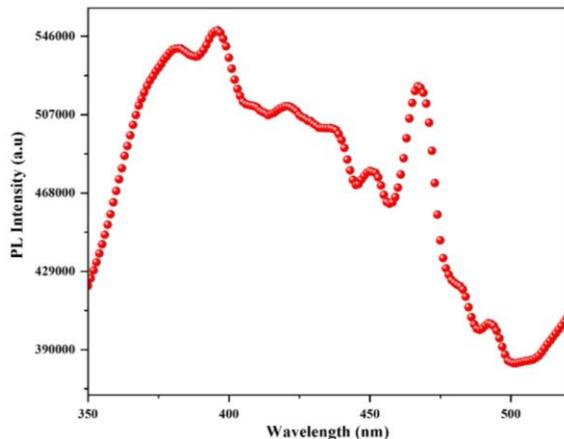Fig. 6:   a. SEM images of the CCU powders annealed at 800 °C, b. EDS spectra of the as prepared sample.

Fig. 7: PL spectrum of CeO$_2$-CuO prepared by self-combustion.

Fig. 8 shows the spectrum of reflectance (%) as a function of the wave length (nm) for the as-prepared sample in the 200-800 nm range. Using the KM function, the Eg value is determined by extra polating the linear portion of the plot relating $(\alpha h\vartheta)^2$ (Kubelka-Munk function) versus $h\vartheta$ to $(\alpha h\vartheta)^2 = 0$ (Kubelka-Munk conversion spectrum) [47].

The optical band gap was estimated to be equal to E_g= 2.05 eV. By comparing this result with the band gap of pure CuO reported by the works of Sedefoglu *et al* [48] and Baglari *et al* [49] 1,3 and 1,5 eV respectively ,and pure CeO$_2$ band gap calculated by kumaran *et al* [50] and Fudala *et al* [51] 3,06 eV and 3,35 eV respectively.

The value of the gap obtained equal to the average value of the band gap for the two oxides, this value it's the same calculated by the works of [52].

BET analysis

N$_2$ adsorption/desorption isotherm of the sample are shown in Fig. 9. The isotherm shape depends on the physicochemical properties and the solid's porous texture [53-55].

According to the IUPAC classification, at high relative pressures, the isotherm is type IV isotherm with H3 type hysteresis loop.

Fig. 9 also exhibits the distribution of pore size determined from the isotherm using the BJH approach, indicating that this sample was classified as mesopore structures with pore diameters varying from 2 to 50 nm.
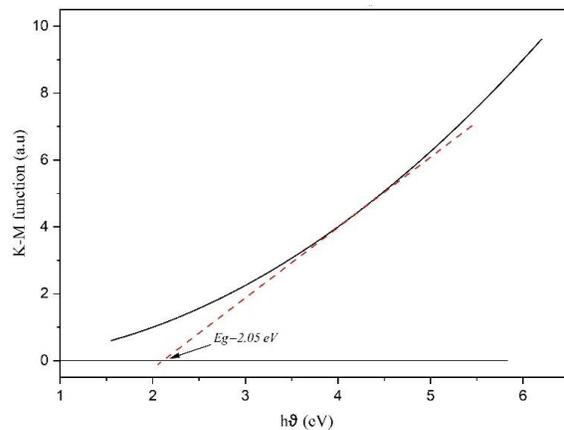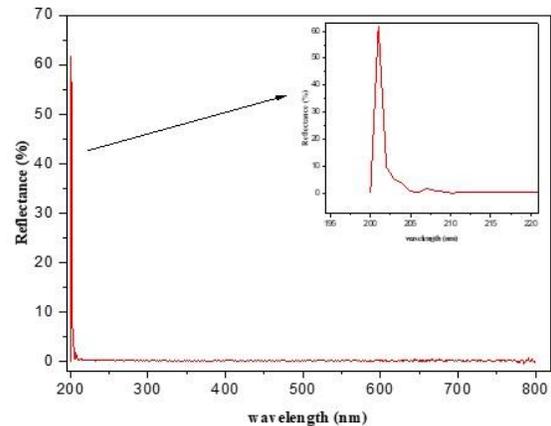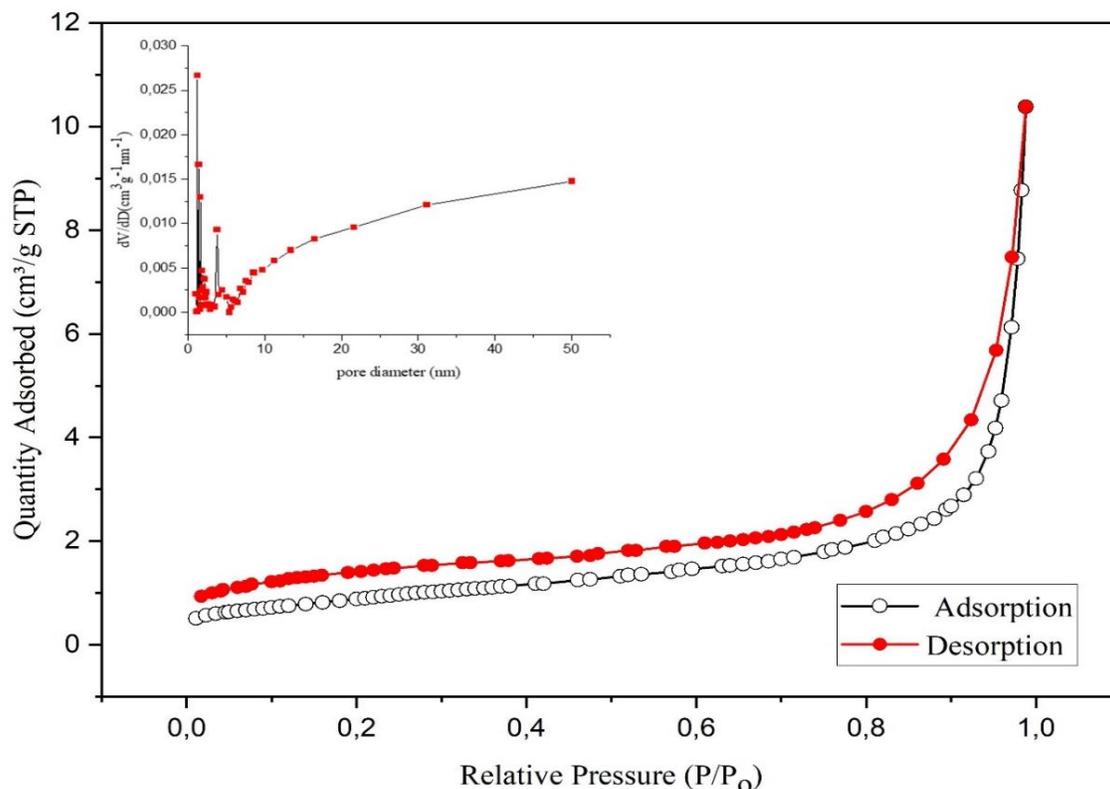

Fig. 8: UV-Visible reflectance spectra and graphic for band gap estimation of CeO$_2$-CuO.

Based on the observed sample morphology, the pores are dispersed between 5 and 10 nm. The formation of the smaller pores was due to the aggregation of the microscopic crystal grains.

The S$_{BET}$, the average pore diameter, and the total pore volume calculated from the isotherm are summarized in Table-3. The value of S$_{BET}$ of synthesized CCU is 3.33 m^2/g. This value is less folded than that broken by Sangsefidi *et al*. [56] (85.10 m^2/g), which prepared the binary composite by green synthesis and under calcination at 500 °C for 4 h. Moreover, that of Cam *et al*. [57] (46.00 m^2/g), which synthesized the CCU by the combustion method using urea as a combustion agent and calcined at 500°C for 2 h. This small value of S$_{BET}$ can be due to the very high temperature of calcination (800 °C) compared to the works cited in [56] and [67].

Table-3: Main textural properties of CeO$_2$-CuO sample.

Sample	BET surface (m²/g)	Average pore diameter (nm)	Total pore volume (cm³/g)
CCU	3.3	13.9	0.0115

Fig. 9:   N$_2$ adsorption/desorption isotherms and pore size distribution curves of the CCU composite.

TPR analysis:

On the TPR curves of the studied system (Fig. 10), the appearance of reduction peaks was noted. One very low intensity was observed towards 366°C and the other one of high intensity located at 250°C. According to previous studies [58, 59, 60] these peaks of hydrogen consumption on the sample correspond to the reduction of CuO particles interacting with CeO$_2$.
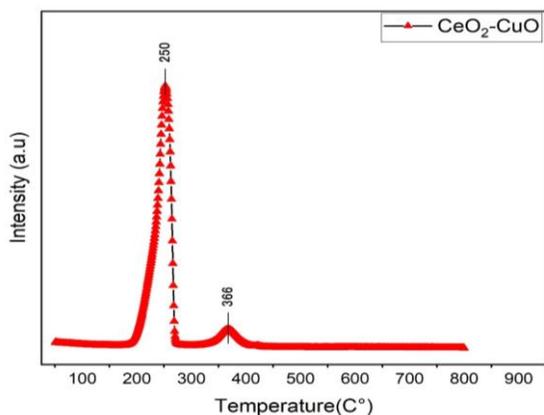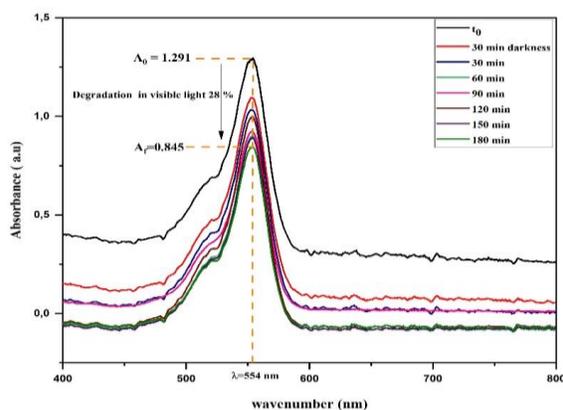
Photocatalytic Activity:

The photocatalytic performance of the as-prepared material was determined by measuring the absorbance of solutions containing Rhodamine B as targeted dyes and the powder of the prepared material as photocatalyst irradiated by visible light for fixed time intervals at 30 minutes. The variation of the absorbance of the previous irradiated solutions in function with time are plotted in Fig.11- a. It is apparent that the absorbance is decreased gradually to reach (A= 0,845 at 554 nm) where the removal efficiency up to 28% after 3 hours, indicating a slow and limited photocatalytic activity. Fig.11- b illustrates the evaluation of RhB concentration (Ct/C0) versus time of irradiation where 28 % of the initial concentration was removed by photocatalytic degradation.

Recyclability

The recycling tests were carried out to study the recyclability of CeO$_2$/CuO photocatalyst.
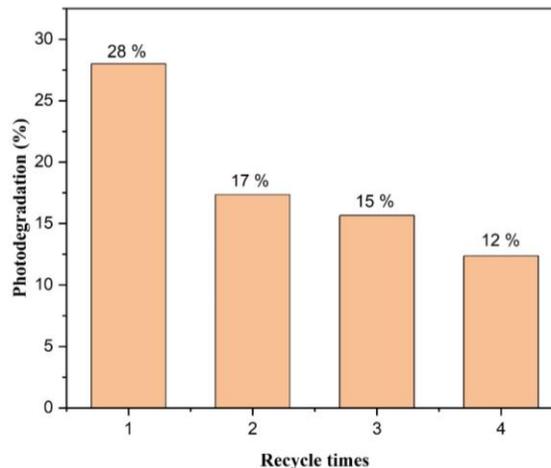
After each photocatalytic reaction, the CeO$_2$/CuO photocatalyst was centrifugated and rinced with distilled water and then ethanol for reuse. The second cycle was initiated with the same conditions (0.5mg/1ml), irradiation time and lamps (4*3W). Four cycles reduced the elimination rate from 28% to 12%, as seen in Fig. 12.

Fig. 10: H_2-TPR profiles of the CeO_2-CuO sample.

Fig. 12: Recycling of the CeO_2/CuO for photodegradation of RhB.

Fig. 11: a- Photocatalytic activity of CeO_2/CuO NPs sample under visible light irradiation, b- the evaluation of RhB concentration (Ct/C0) versus time of irradiation.

Conclusion

An auto combustion method successfully generated a CeO_2/CuO composite oxide (CCU) for photocatalytic degradation of Rhodamine B dye under visible light. Various techniques including XRD, TGA, SEM and BET were adopted to characterize the CCU produced and study the structural, optical and morphological properties. According to the XRD characterization and using the preliminary characterization of the precursor by TGA, the formation of a binary composite CCU was obtained at 800 °C under monoclinic and cubic systems with 40 and 65 nm an average particle size for CuO and CeO_2 respectively. SEM analysis of the sample morphology shows large agglomerates with non-uniform forms of particles. While the CCU used to have a surface area of 3.33 m^2/g.

The photocatalytic activity of the prepared oxide was tested by degrading RhB under LED lamps (visible light) of 12 w for 180 min where a 28 % degradation rate was obtained. The removal ration decreased from 28% to 12% after four cycles using the same procedure after each cycle, Degradation is slow and limiting. This result is acceptable if we consider that, there is no work on the degradation of RhB by CCU and without forgetting that RhB is classified among the most difficult dyes to degrade.

Acknowledgment

References

1. O. Baaloudj, H. Kenfoud, A. K. Badawi, A. A. Assadi, A. El Jey, A. A. Assadi and A. Amrane, Bismuth Sillenite Crystals as Recent Photocatalysts for Water Treatment and Energy Generation: A Critical Review, *Catalysts*, **12**, 500 (2022).

2. B. Ismail, S. T. Hussain and S. Akram, Adsorption of Methylene Blue Onto Spinel Magnesium Aluminate Nanoparticles: Adsorption Isotherms,Kenitic and Thermodynamic Studies, *Cheml Eng J*, **219**, 395 (2013).

3. J. S. Piccin, C. S. Gomes, L. A. Feris, and M. Gutterres, Kinetics and Isotherms of Leather Dye Adsorption by Tennery Solid Waste, *Chem Eng J*, **183**, 30 (2012).

4. M. Y. Nassar, I. S. Ahmed, and I. Samir, A Novel Synthetic Route for Magnesium Aluminate ($MgAl_2O_4$) Nanoparticles Using Sol-Gel Auto Combustion Method and Their Photocatalytic Properties, *Spec. chim Acta Part A: Mol & Biomol Spec,* **131**, 329 (2014).

5. S. Vigneshwaran,C. M. Park and S. Meenakshi, Designed Fabrication of Sulfide-Rich Bi-Metallic-Assembled Mxene Layred Sheets with Dramatically Enhanced Photocatalytic Performance for Rhodamine B Removal,*Sep & Pru Tech*, **258**, 118003 (2021).

6. Z. Wessely, S. H. Shapiro, J. V. Klavins and H. M. Tinberg, Identification of Mallory Bodies with Rhodamine B Fluorescence and other Sains for Stains for Keratin, *S Tech*, **56**, 169 (1981).

7. S. H. Shapiro and Z. L. M. A. Wessely, Rhodamine B Fluorescence as A Stain for Amniotic Fluid Squames in Maternal Pulmonary Embolism and Fetal Lungs, *Ann of Cli & Lab Sci*, **18**, 451 (1988).

8. H. Cui, S. Dong, K. Wang, M. Luan and T. Huang, Synthesis of A Novel Type-Ii In_2S_3/Bi_2MoO_6 Heterojunction Photocatalyst: Excellent Photocatalytic Performance and Degradation Mechanism for Rhodamine B, *Sep & Pur Tech*, **255**, 117758 (2021).

9. M. Ahmad, W. Rehman, M. M. Khan, M. T. Qureshi, A. Gul, S. Haq and F. Menaa, Phytogenic Fabrication of ZnO and Gold Decorated ZnO Nanoparticles For Photocatalytic Degradation Of Rhodamine B. *J Env Chem Eng*, **9**, 104725 (2021).

10. S. P. Vattikuti, K. C. Devarayapalli, N. K. Reddy Nallabala, Nguyen, N. Nguyen Dang and J. Shim, Onion-Ring-Like Carbon And Nitrogen From Zif-8 On TiO_2/Fe_2O_3 Nanostructure for Overall Electrochemical Water Splitting, *The J Phy Chem Let*, **12**, 5909 (2021).

11. M. Mousavi-Kamazani, Facile Sonochemical-Assisted Synthesis of $Cu/ZnO/Al_2O_3$ Nanocomposites under Vacuum: Optical and Photocatalytic Studies, *Ultrasonics Sonochemistry*, **58**, 104636 (2019).

12. Y. He, N. B. Sutton, H. H. Rijnaarts and A. A. Langenhoff, Degradation of Pharmaceuticals in Wastewater Using Immobilized TiO_2 Photocatalysis under Simulated Solar Irradiation, *App Cat B: Env*, **182**, 132 (2016).

13. Y. Huang, F. Sun, T. Wu, Q. Wu, Z. Huang, H. Su and Z. Zhang, Photochemical Preparation of CdS Hollow Microspheres at Room Temperature and Their Use in Visible-Light Photocatalysis, *J S S Chem*, **184**, 644 (2011).

14. S. Malato, P. Fernández-Ibáñez, M. I. Maldonado, J. Blanco and W. Gernjak, Decontamination and Disinfection of Water by Solar Photocatalysis: Recent Overview a nd Trends, *Catalysis Today*, **147**, 1 (2009).

15. H. Tong, S. Ouyang, Y. Bi, N. Umezawa, M. Oshikiri and J. Ye, Nano-Photocatalytic Materials: Possibilities and Challenges. *Adv Mat*, **24**, 229 (2012).

16. M. A. Subhan, N. Uddin, P. Sarker, A. K. Azad and K. Begum, Photoluminescence, Photocatalytic and Antibacterial Activities of CeO_2-CuO-ZnO Nanocomposite Fabricated by Co-Precipitation Method, *Spectrochimica Acta Part A: Mol & Biomol Spe*, **149**, 839 (2015).

17. P. Bera, A. Gayen, M. S. Hegde, N. P. Lalla, L. Spadaro, F. Frusteri and F. Arena, Promoting Effect of CeO_2 in Combustion Synthesized Pt/CeO_2 Catalyst for Co Oxidation, *J Phy Chem B*, **107**, 6122 (2003).

18. G. Jacobs, L. Williams, U. Graham, D. Sparks and B. H. Davis, Low-Temperature Water-Gas Shift: In-Situ Drifts− Reaction Study of A Pt/CeO_2 Catalyst for Fuel Cell Reformer Applications,*J Phys Chem B*, **107**, 10398 (2003).

19. K. Sohlberg, S. T. Pantelides and S. J. Pennycook, Interactions of Hydrogen with CeO_2, *J A Chem Soc*, **123**, 66091 (2001).

20. Fauzi, A. A., Jalil, A. A., Hassan, N. S., Aziz, F. F. A., Azami, M. S., Hussain, I., ... & Vo, D. V. A critical review on relationship of CeO_2-based photocatalyst towards mechanistic degradation of organic pollutant. *Chemosphere*, **286**, 131651 (2022).

21. A. Trovarelli, Catalytic Properties of Ceria and CeO_2-Containing Materials. *Cat Rev*, **38,** 439 (1996).

22. S. Colussi, C. De Leitenburg, G. Dolcetti and A. Trovarelli, The Role of Rare Earth Oxides as Promoters and Stabilizers in Combustion Catalysts, *J Alloys & Comp*, **374**, 387 (2004).

23. T. Masui, T. Ozaki, K. I. Machida and G. Y. Adachi, Preparation of Ceria–Zirconia Sub-Catalysts for Automotive Exhaust Cleaning, *J Alloys & Comp*, **303**, 49 (2000).

24. X. Wang, J. A. Rodriguez, J. C. Hanson, D. Gamarra, A. Martínez-Arias and M. Fernández-García, in Situ Studies of the Active Sites for the Water Gas Shift Reaction Over Cu– CeO_2 Catalysts : Complex Interaction Between Metallic Copper and Oxygen Vacancies of Ceria, *J Phy Chem* B, **110**, 428 (2006).

25. N. Indumathi, C. Sridevi, A. Gowdhaman, and R. Ramesh, Synthesis, structural analysis, and electrochemical performance of Chitosan incorporated CuO nanomaterial for supercapacitor applications. *Inorg Chem Com,* 111222. (2023).

26. A. L. Jadhav and S. M. Khetre, Antibacterial Activity of $LaNiO_3$ Prepared by Sonicated Sol-Gel Method Using Combination Fuel, *Inter Nano Let*, **10**, 23 (2020).

27. J. D. Fernandes, D. M. D. A. Melo, L. B. Zinner, C. D. M. Salustiano, Z. R. Silva, A. E. Martinelli, ... and M. I. B. Bernardi, Low-Temperature Synthesis of Single-Phase Crystalline $LaNiO_3$ Perovskite Via Pechini Method, *Mat Letters*, **53**, 122 (2002).

28. S. K. Chawl, M. George, F. Patel and S. Patel, Production of Synthesis Gas by Carbon Dioxide Reforming of Methane Over Nickel Based and Perovskite Catalysts, *Pro Eng*, **51**, 461 (2013).

29. S. L. González-Cortés and F. E. Imbert, Fundamentals, Properties and Applications of Solid Catalysts Prepared by Solution Combustion Synthesis (Scs), *App Cat A: G*, **452**, 117 (2013).

30. A. S. Mukasyan, Solution Combustion as a Promising Method for the Synthesis of Nanomaterials. *Adv Sci & Tech*, **63**, 187 (2010).

31. E. A. Zaboeva, S. G. Izotova, and V. I. Popkov, Glycine-nitrate combustion synthesis of $CeFeO_3$-based nanocrystalline powders. *R J App Chem*, **89**, 1228 (2016).

32. R. David Lide, Ed., Crc Handbook of Chemistry and Physics, Crc Press/Taylor and Francis, Boca Raton, Fl, 89th Edition (Internet Version 2009).

33. D. Faical, A. Martínez-Arias, and M. Gurgan, Effect of the Synthesis Method, Complexing Agent and Solvent on the Physicochemical Properties of $LaNiO_3$ Nanopowders. *J Chem Soc Pak*, **44**, 3 (2022).

34. E. Omari and M. Omari, Synthesis and Electrocatalytic Properties of $LaFe_{1-X}Zn_xO_3$ Perovskites, *J Sol-Gel Sci & Tech*, **96**, 219 (2020).

35. A. Sharma and P. S. Kumar, Synthesis and Characterization of CeO-ZnO *Nanocomposites. Nano sci & Nano tech*, **2**, 82 (2012).

36. M. Mousavi-Kamazani, Z. Zarghami, and M. Salavati-Niasari, Facile and novel chemical synthesis, characterization, and formation mechanism of copper sulfide (Cu_2S, Cu_2S/CuS, CuS) nanostructures for increasing the efficiency of solar cells. *J Phy Chem C*, **120**, 2096 (2016).

37. M. Mousavi-Kamazani, R. Rahmatolahzadeh, and F. Beshkar, Facile solvothermal synthesis of CeO_2–CuO nanocomposite photocatalyst using novel precursors with enhanced photocatalytic performance in dye degradation. *J Inorg & Org Poly & Mat*, **27**, 1342 (2017).

38. J. Hammouche, M. Gaidi, S. Columbus and M. Omari, Enhanced Photocatalytic Performance of Zinc Ferrite Nanocomposites for Degrading Methylene Blue: Effect of Nickel Doping Concentration, *J Inorg & Org Poly & Mat*, **31**, 3496 (2021).

39. S. f. Khyrun, A. J. Christy, R. Usha, L. C. Nehru, and S. Suresh, Novel solution combustion synthesis of CeO_2/CuO nanocomposite for photocatalytic and biological applications. *Op Mat*, **139**, 113756 (2023).

40. E. C. C. Souza, H. F. D. Brito, and E. N. D. S. Muccillo, Optical and electrical characterization of samaria-doped ceria. *J alloys & comp*, **491**, 460 (2010).

41. A. A. Khosravi, M. Kundu, L. Jatwa, S. K. Deshpande, U. A. Bhagwat, M. Sastry, and Kulkarni, Green luminescence from copper doped zinc sulphide quantum particles. *App Phys Letters*, **67**, 2702 (1995).

42. S. Baglari, R. R. Wary, P. Kalita, and M. B. Baruah, Green synthesis of CuO nanoparticles using citrus maxima peel aqueous extract. *Mat T: Proc* (2023).

43. Z. R. Parekh, S. H. Chaki, A. B. Hirpara, G. H. Patel, Kannaujiya, A. J. Khimani, andM. P. Deshpande, CuO nanoparticles–synthesis by wet precipitation technique and its characterization. *Phys B: Cond Mat*, **610**, 412950 (2021).

44. G. Manibalan, G. Murugadoss, R. Thangamuthu, P. Ragupathy, R. M. Kumar, and R. Jayavel, Enhanced electrochemical supercapacitor and excellent amperometric sensor performance of

heterostructure CeO_2-CuO nanocomposites via chemical route. *App Sur Sci*, **456**, 104 (2018).

45. G. Manibalan, G. Murugadoss, R. Thangamuthu, P. Ragupathy, R. M. Kumar and R. Jayavel, Enhanced Electrochemical Supercapacitor and Excellent Amperometric Sensor Performance of Heterostructure CeO_2-CuO Nanocomposites Via Chemical Route, *App Sur Sci*, **456**, 104 (2018).

46. A. B. Murphy, Band-Gap Determination from Diffuse Reflectance Measurements of Semiconductor Films, and Application to Photoelectrochemical Water-Splitting, *Sol E Mat & Sol Cells*, **91**, 1326 (2007).

47. J. Tang, Z. Zou and J. Ye, Efficient Photocatalysis on $BaBiO_3$ Driven by Visible Light, *Journal Phy Chem* C, **111**, 12779 (2007).

48. N. Sedefoglu, S. Er, Veryer, K., Zalaoglu, and F. Bozok, Green synthesized CuO nanoparticles using macrofungi extracts: Characterization, nanofertilizer and antibacterial effects. *Mat Chem &Phy*, 128393 (2023).

49. S. Baglari, R. R. Wary, P. Kalita, and M. B. Baruah, Green synthesis of CuO nanoparticles using citrus maxima peel aqueous extract. *Mat T: Pro*. (2023).

50. C. Kumaran, I. Baskaran, B. Sathyaseelan, K. Senthilnathan, E. Manikandan, and S. Sambasivam, Effect of doping of iron on structural, optical and magnetic properties of CeO_2 nanoparticles. *Chem Phy Letters*, **808**, 140110 (2022).

51. A. S. Fudala, W. M. Salih, and F. F. Alkazaz, Synthesis different sizes of cerium oxide CeO_2 nanoparticles by using different concentrations of precursor via sol–gel method. *Mat T: Pro*, **49**, 2786 (2022).

52. A. A. Baqer, K. A. Matori, N. M. Al-Hada, A. H. Shaari, H. M. Kamari, E. Saion, C. A. C. Abdullah, Synthesis and characterization of binary $(CuO)_{0.6}$ $(CeO_2)_{0.4}$ nanoparticles via a

simple heat treatment method. *R Phy*, **9**, 471 (2018).

53. H. J. Butt, K. Graf and M. Kappl, Physics and Chemistry of Interfaces. *John Wiley & Sons* (2013).

54. G. Leofanti, M. Padovan, G. Tozzola and B. J. C. T. Venturelli, Surface Area and Pore Texture of Catalysts. *Cat T*, **41**, 207 (1998).

55. K. S. Sing, Reporting Physisorption Data for Gas/Solid Systems with Special Reference to the Determination of Surface Area and Porosity (Recommendations 1984), *Pure & App Chem*, **57**, 603 (1985).

56. F. S. Sangsefidi, M. Salavati-Niasari, H. Khojasteh, M. Shabani-Nooshabadi, Synthesis, characterization and investigation of the electrochemical hydrogen storage properties of $CuO–CeO_2$ nanocomposites synthesized by green method. *Inter J of Hyd Energy*, **42,** 14608 (2017).

57. T. S. Cam, A. E. Petrova, V. L. Ugolkov, D. A. Sladkovskiy, and V. I. Popkov, On the SCS Approach to the CeO_2/CuO Nanocomposite: Thermochemical Aspects and Catalytic Activity in n-Hexane Conversion. *Rus J Inorg Chem,* **65**, 725 (2020).

58. X. Yan, A. Zhang, M. Gao and S. Zeng, CeO_2/CuO Catalysts Using Different Template Agent for Preferential Co Oxidation in H_2-Rich Stream, *J Rare Earths*, **35**, 1216 (2017).

59. S. Zeng, K. Liu, L. Zhang, B. Qin, T. Chen, Y. Yin and H. Su, Deactivation Analyses of CeO_2/CuO Catalysts in the Preferential Oxidation of Carbon Monoxide, *J Power Sour*, **261**, 46 (2014).

60. Y. Yin, K. Liu, M. Gao, L. Zhang, H. Su and S. Zeng, Influence of the Structure and Morphology of CuO Supports on the Amount and Properties of Copper–Cerium Interfacial Sites in Inverse CeO_2/CuO Catalysts, *J Mol Cat* A: *Chem*, **404**, 193 (2015).